



Experimental Investigation of Vortex Generator Effect on Two- and Three-Dimensional NASA Common Research Models

Shunsuke Koike¹, Kazuyuki Nakakita², Tsutomu Nakajima³, Seigo Koga⁴, Mamoru Sato⁵, Hiroshi Kanda⁶, Kazuhiro Kusunose⁷, Mitsuhiro Murayama⁸, Yasushi Ito⁹, and Kazuomi Yamamoto¹⁰
Japan Aerospace Exploration Agency, Chofu, Tokyo, 182-8522

Aerodynamic characteristics of two- and three-dimensional NASA common research model (2D-CRM and 3D-CRM) with co-rotating vortex generators (VGs) were investigated to clarify the influence of the three-dimensionality of the wings on the VGs effect. The base height of the VGs was 1.5 times of the boundary layer thickness at the VGs location. The direction of the VGs on the 3D-CRM was toe-out which meant the leading edge of the VGs turned to the wing tip. The Mach numbers in the 2D- and 3D-CRM experiment were 0.74 and 0.85 considering the sweepback angle of the 3D-CRM. The lift coefficient and the oil flow visualization showed that the effect of the VGs on the 3D-CRM was much larger than that on the 2D-CRM. From the comparison between the experiments and the CFD results, we concluded that the difference between 2D- and 3D-CRM was mainly caused by the cross-flow due to the swept wing. The cross-flow enhances the effect of the co-rotating toe-out VGs on the swept wings. The installation drag of VGs was also investigated for the 3D-CRM and validated an empirical method to estimate the installation drag. At C_L conditions below the design $C_L = 0.5$, the VGs increased the total drag as expected, while at C_L conditions above the design C_L , the VGs decreased the total drag because the VGs suppressed the separation and the effect exceeded the installation drag of the VGs.

Nomenclature

AoA = angle of attack
 AR = aspect ratio of vortex generator defined by Eq. (11)
 Av = angle of vortex generators

¹ Researcher, Institute of Aeronautical Technology, 7-44-1 Jindaiji-Higashi, Chofu, Tokyo, 182-8522, Japan, Member AIAA.

² Senior Researcher, Institute of Aeronautical Technology, 7-44-1 Jindaiji-Higashi, Chofu, Tokyo, 182-8522, Japan, Senior Member AIAA.

³ Researcher, Institute of Aeronautical Technology, 7-44-1 Jindaiji-Higashi, Chofu, Tokyo, 182-8522, Japan, Non-Member AIAA.

⁴ Engineer, Institute of Aeronautical Technology, 7-44-1 Jindaiji-Higashi, Chofu, Tokyo, 182-8522, Japan, Member AIAA.

⁵ Associate Senior Researcher, Institute of Aeronautical Technology, 7-44-1 Jindaiji-Higashi, Chofu, Tokyo, 182-8522, Japan, Non-Member AIAA.

⁶ Associate Senior Researcher, Institute of Aeronautical Technology, 7-44-1 Jindaiji-Higashi, Chofu, Tokyo, 182-8522, Japan, Non-Member AIAA.

⁷ Visiting Researcher, Institute of Aeronautical Technology, 7-44-1 Jindaiji-Higashi, Chofu, Tokyo, 182-8522, Japan, Non-Member AIAA.

⁸ Associate Senior Researcher, Institute of Aeronautical Technology, 6-13-1 Osawa, Mitaka, Tokyo 181-0015, Japan, Senior Member AIAA.

⁹ Researcher, Institute of Aeronautical Technology, 6-13-1 Osawa, Mitaka, Tokyo 181-0015, Japan, Senior Member AIAA.

¹⁰ Associate Principal Researcher, Institute of Aeronautical Technology, 6-13-1 Osawa, Mitaka, Tokyo 181-0015, Japan, Senior Member AIAA.

b	=	span length
C	=	chord length
C_C	=	coefficient of axial force
C_D	=	drag coefficient
$C_{D_{vg}}$	=	drag coefficient of isolated vortex generator on a flat plate wing
C_L	=	lift coefficient
C_m	=	pitching moment coefficient
C_N	=	coefficient of normal force
C_p	=	pressure coefficient
D_v	=	distance between adjacent vortex generators
H_v	=	height of vortex generator
i	=	number of pressure taps of 2D-CRM
L_v	=	length of vortex generator
m_{vg}	=	magnification factor for isolated vortex generator
M	=	Mach number
n_i	=	total number of pressure taps of 2D-CRM
N_{VG}	=	number of vortex generators on half wing
p	=	static pressure
p_0	=	total pressure
q	=	dynamic pressure
Re	=	Reynolds number
S	=	reference area
S_{vg}	=	area of isolated vortex generator
U	=	velocity
x	=	coordinate of uniform flow direction
X_v	=	location of vortex generators in chord direction
y	=	coordinate of spanwise direction
z	=	coordinate of height direction
α_{vg}	=	angle of vortex generator to the flow direction ($= A_v$)
δ	=	99% boundary layer thickness at vortex generator location
$\Delta C_{D_{vg}}$	=	installation drag of isolated vortex generator
η	=	fraction of wing semi-span ($= y / (b/2)$)

Subscript

$Clean$	=	physical properties in the case without vortex generators
TE	=	physical properties at trailing edge
vg	=	physical properties of isolated vortex generator or at the location of vortex generator
VG	=	physical properties in the case with vortex generators
∞	=	physical properties of uniform flow

I. Introduction

Vortex generators (VGs) are aerodynamic devices which produce streamwise vortices. Those streamwise vortices entrain the outer flow into the boundary layer and improve velocity profile in the boundary layer. Consequently, the VGs suppress the undesired separation and improve the performance of aerodynamic devices. In this research, we focus on the VGs which suppress the shock induced separation in transonic flow. Those VGs are effective for the suppression of flow separation and the shock wave oscillation^{1,2}. Hence many aircraft have those VGs on their wings to increase the cruise speed and to allow more flight maneuvers. Although those VGs have been used for aircraft for a long time and several design guidelines³⁻⁵ have been reported, their basic physics has not been fully understood. The parameter of the VGs, height, length, interval, location, and angle are often designed empirically. Objective of this research is to understand the physics of the VGs effects, and to acquire guidelines of optimal design of VGs on aircraft wings. To efficiently meet the goals, both wind tunnel tests^{6,7} and Computational Fluid Dynamics (CFD) simulations⁸⁻¹⁰ have been conducted.

In this paper, the results of the wind tunnel tests are reported. To examine the influence of wing three-dimensionality on the VGs effect, the experiment was conducted using a two dimensional airfoil of the NASA common research model (2D-CRM)¹¹ and a JAXA's 80% scale NASA Common Research Model (3D-CRM)¹²⁻¹⁷.

The effect of the rectangular co-rotating VGs on the lift force was compared between 2D- and 3D-CRM cases. Flow visualization was also conducted in both experiments to clarify the flow fields produce by the VGs. In order to investigate the penalty of the VGs, the installation drag of the VGs was also investigated for the 3D-CRM. The results of the CFD related to the present experiments are reported in the companion paper¹⁰ by Ito et al.

Although the influence of several parameters of VGs were investigated for the 2D-CRM, only the influence of the height and the interval of VGs are described in this paper to focus on the comparison between the 2D- and 3D-CRM. The influences of the other parameters of VGs on the 2D-CRM and a NASA SC(2)-0518¹⁸ airfoil which had no sweepback angle were shown in Ref.7. The VGs effect on the NASA SC(2)-0518 was qualitatively same as that on the 2D-CRM for the parameters of the height and the interval of VGs. Based on these comparisons, we conducted the experiments for the 3D-CRM in this research.

A. Experiment of 2D-CRM

1. 2D-CRM

Figure 1 shows the airfoil of the 2D-CRM¹¹. It was based on the airfoil of the 3D-CRM at $\eta = 65\%$ considering the sweepback angle of 31.5 degrees. The trailing edge was blunt. The chord and span length were 200 mm and 450 mm, respectively. Sweepback angle was zero. Main material of the model was stainless steel (HPM38).

The position of the pressure taps were shown as the circle symbols in Fig. 1. The 2D-CRM had three lines of the pressure taps on the upper surface and one line of those on the lower surface in the chord direction. The model also had a line of the pressure taps in the spanwise direction at $x/C = 94\%$. The total number of the pressure taps was 80.

In order to produce turbulent boundary layer, lines of disk roughness (Aeronautical Trip Dots, 3.1 mil Silver matte, CAD Cut inc.) were attached at $x/C = 10\%$ on the upper and on the lower surface of the model. The height of the roughness was 0.0031 inch (79 μm) which was a little higher than the height of the estimation using the method in Ref. 19. The diameter and interval of the roughness disks were 0.05 inch and 0.1 inch, respectively.

2. Wind Tunnel

The experiments of the 2D-CRM were conducted in JAXA 0.8m x 0.45m high Reynolds number transonic wind tunnel (JTWT2)^{20, 21}. Figure 2 presents the JTWT2. The JTWT2 is a high pressure blow down wind tunnel. The height and width of the test section were 800 mm and 450 mm, respectively. The top and bottom walls have slots to realize the transonic flow conditions.

The model was supported by both ends using supporters. There was no gap between the model and the side walls. To reduce the influence of the side walls, the boundary layer on the side walls was evacuated through the rigimesh plates upstream of the airfoil model. In this evacuation, an ejector system was used to increase the suction mass flow rate.

The design Mach number of the 3D-CRM was 0.85. Considering the effect of the sweepback angle of the 3D-CRM and the interference of the wind tunnel walls, the nominal Mach number before the wall interference correction was determined as 0.74. The averaged Mach number after the wall interference correction was 0.736. The nominal Reynolds number based on the chord length was 5×10^6 . The Reynolds number of 5×10^6 was same as that of the NASA's CRM experiments for forth drag prediction workshops (DPW-4)¹². On this condition, duration time of the wind tunnel experiment was 60 s. The data for the six angles of attack were measured in one blow.

3. Vortex Generators

The effect of rectangular co-rotating VGs was investigated in this experiment. Figure 3 shows the shape and the parameters of VGs. Table 1 presents the experimental conditions for the 2D-CRM. Figure 4 shows the photos of the VGs and the 2D-CRM.

A line of the rectangular VGs was installed at X_v/C of 0.2. The heights of VGs H_v were 1.2 mm and 2.4 mm. The height of 1.2 mm was 1.5 times of the boundary layer thickness δ at the location of the VGs. The boundary layer thickness was estimated from CFD result. The deviation from the specified height of VGs was less than 0.05 mm. The VGs were made of stainless steel whose thickness was 0.1 mm. The lengths of VGs L_v were 4 times of the heights. The angle of VGs to the uniform flow direction A_v was 20 degrees. The leading edge of all VGs turned to the left side. The intervals of adjacent VGs D_v were 10, 20, and 40 times of the VGs height. The relation between the VGs and pressure taps are shown in Fig. 1. The triangle symbols in Fig. 1 show the VGs location when the D_v/H_v was 10. The VGs on the center line ($y = 0$ mm) remained for all cases.

Generally, the size of VGs in the wind tunnel experiment is small since models are much smaller than the real wings. One of the difficulties of the VGs experiment is how to precisely attach the small VGs to the wing model and how to easily detach them in order to examine the many configurations of the line of VGs. The enough adhesive strength is also needed to withstand the aerodynamic force. In order to realize the wind tunnel experiment, we used a

jig and an acrylic-based adhesive (SKYLOCK RD-57G, VA-05, NIKKA SEIKO). The adhesive strength was 22.5 N/mm². The VGs attached with the acrylic-based adhesive was easily detached with hot water. Details of the VGs installation are described in Ref. 6 and 7.

4. Measurement Techniques

The effect of the VGs was quantitatively investigated from the pressure distributions on the airfoil. The pressure from the 80 ports on the airfoil surface was measured with scanning-type pressure gauge. The uncertainty of the C_p was less than 0.02 except the region close to a shock wave and it was about 0.2 around the shock wave location. Pressure coefficients C_p , Mach number M , angle of attack AoA , and lift coefficient C_L were corrected by Sawada's method^{22, 23} to eliminate the influence of the interference of top and bottom wall. In order to use Sawada's method, the static pressure on the top and bottom wall were measured with the static pressure rails. The pressure was measured at sampling rate of 1 ms. 20 points were sampled and averaged for the each pressure port. Since the response rate of the pressure measurement system was too slow, time resolved pressure data could not been obtained. However, the averaged pressure distributions clearly revealed the VGs effect as described in the section of results. In order to easily compare the VGs effect, the lift coefficients were calculated from the pressure distribution on the surface of the airfoil using the following equations. Here, i is the number of the pressure port. The order of the number i is as follows, leading edge - upper surface - trailing edge - lower surface - leading edge.

$$C_L = C_N \cos(AoA) - C_C \sin(AoA) \quad (1)$$

$$C_N = \frac{-1}{2C} \sum_{i=1}^{n_i} [C_p(i+1) + C_p(i)] \times [x(i+1) - x(i)] \quad (2)$$

$$C_C = \frac{-1}{2C} \sum_{i=1}^{n_i} [C_p(i+1) + C_p(i)] \times [z(i+1) - z(i)] \quad (3)$$

The uncertainty of the lift coefficient C_L was less than 0.02 except the correction error of the wall interference. As described in Ref. 23, Sawada's correction method is not appropriate when the lift slope is not linear. Hence, strictly speaking, the corrected values under the shock wave oscillating condition have the correction error. However, the corrected values are shown in this paper in order to continuously show the data plot. The correction does not change the evaluation of the VGs effect in this experiment. The uncorrected values are suitably mentioned to clearly show the experimental conditions.

Oil flow visualization technique was used to investigate the flow pattern on the suction surface of the wing. The oil consisted of liquid paraffin, titanium dioxide as a dye, and a little oleic acid. The color of dye was white. The visualization data were recorded with a video camera mounted outside the test section on the top wall in the plenum chamber. The behavior of the oil pattern during each run was recorded continuously and specific scenes were captured from the movie data.

Color schlieren technique was used to visualize the shock waves and the expansion waves on the airfoil. The diameter of the concaved mirror was 300 mm. The light source was a xenon lamp. The schlieren images were recorded by a video camera. The recording was conducted both in the pressure measurement and in the oil flow visualization. Schlieren images were useful to monitor the flow and the model conditions.

B. Experiment of 3D-CRM

1. JAXA's 80 % Scale NASA CRM

The NASA CRM consists of a contemporary supercritical transonic wing and a fuselage representative of a wide body commercial transport aircraft. The design Mach number and lift coefficient are 0.85 and 0.5, respectively, at a Reynolds number of 40×10^6 . Details of the model are explained in Ref. 12 and on a web site¹³ prepared by NASA's Langley Research Center (LaRC).

The JAXA CRM wind tunnel model (3D-CRM) is an 80 % scale of NASA's wind tunnel model. Its size corresponds to 2.16 % of the assumed scale of the CRM. The model was sized for the JAXA 2m x 2m transonic wind tunnel (JTWT) such that the ratio of the model to the test section size is approximately the same as that for the National Transonic Facility (NTF). Reference area, reference chord, and span are 0.179014 m², 0.15131 m, and 1.26927 m, respectively. Details of the model are explained in Ref. 17.

Figure 5 shows the photos of JAXA's 80 % scale NASA CRM with VGs. The experimental conditions for the model were same as those in Ref. 17. The experiments were conducted in a configuration without the engine nacelles and the pylons. The model was supported by a dorsal sting. The WBT0 (wing/body/tail = 0 deg.) model configuration was selected. In order to produce a turbulent boundary layer on the model surface, disk roughness (Aeronautical Trip Dots, CAD Cut inc.) were attached on the main wings and the horizontal stabilizers at 10% chord length and on the fuselage at 1.5% of its length. The diameter and the distance of adjacent trip dot centers were 0.05 inch and 0.1 inch. The heights were calculated using the method in Ref. 19 with total pressure of 100 kPa. As mentioned below, the total pressure of the experimental conditions was 120 kPa. Hence the height of the trip dots was a little higher than the proper height. The height of the trip dots on the body, outer wings and horizontal stabilizers was 0.0031 inch. The heights on the inner-wings and the mid-wings were 0.0039 inch and 0.0035 inch, respectively.

2. Wind Tunnel

The experiments for the 3D-CRM were conducted in the JTWT. A bird-eye view drawing of the tunnel is shown in Fig. 6. The JTWT is a continuous pressurized wind tunnel. All tests were performed in the tunnel's No. 4 cart which had porous walls. The size of the cart was 2 m in height, 2 m in width, and 4.13 m length. Nominal Mach number was 0.85. Corrected Mach number was a little lower than the nominal Mach number, 0.848. Total pressure and total temperature were 120 kPa and around 50 °C. The resulting nominal Reynolds number was 2.27×10^6 . Although the Reynolds number of 2.27×10^6 was almost the half of the Reynolds number of 5×10^6 in the 2D-CRM experiments, as mentioned below, the experimental conditions of the ratio $Hv/\delta = 1.5$ was fixed in the both experiments in order to make the similarity conditions.

3. Vortex Generators

Table 2 presents the experimental conditions of VGs for the 3D-CRM. The effect of rectangular co-rotating type VGs was investigated in this experiment. The design parameter for the VG geometry and setting was determined at a representative spanwise section on the outer wing where the shock induced flow separation starts as AoA increases. Height of all VGs for the 3D-CRM was 0.8 mm. The height of 0.8 mm was about 1.5 times of the boundary layer thickness δ at the representative spanwise location and about 2 times of δ near the wing tip. The thickness δ was estimated from a CFD result. The ratio Hv/δ of 1.5 is same as that in the case of Hv of 1.2 mm for the 2D-CRM experiments. The lengths of VGs L_V were 4 times of the height H_V . Hence the shape of the VGs for the 3D-CRM was same as that for the 2D-CRM.

The VGs attached on the wing were shown in Fig. 5. The rectangular VGs was installed at a line around X_V/C of 0.2. It was almost same as the location of that in the 2D-CRM experiments. The VGs were attached from $\eta = 0.4$ to the wing tip. The intervals of adjacent VGs D_V were 20, 40, and 80 times of the VGs height. The numbers of the VGs for each case were 23, 12, and 6 for each side of wing. The VGs on the $\eta = 0.4$ remained for all cases.

The direction of the VGs was toe-out which meant the leading edge of the VGs turned to the wing tip. Hence, from the view point of the downstream of the model, the direction of the vortex was clockwise on the right wing and counter clockwise on the left wing. The angle of VGs to the body axis was 32.6 degrees, which corresponds to the flow direction on the wing surface A_V of 20 degrees at the representative spanwise location. $A_V = 20$ degrees was same as the angle in the 2D-CRM experiments.

The VGs were made of stainless steel whose thickness was 0.1 mm. The deviation from the specified height of VGs was less than 0.05 mm. In the same way as the 2D-CRM experiments, we used jigs and an acrylic-based adhesive (SKYLOCK RD-57G, VA-05, NIKKA SEIKO). The experiment was conducted for the three cases decreasing the number of VGs. Unnecessary VGs were detached with hot water to investigate the larger interval case.

4. Measurement Techniques

Figure 7 shows the diagram of the measurement system. The measurement system was same as that in the previous research¹⁷. The balance used in the tests was the TB-M6-04 which was moment-type balance and the most frequently used in the JTWT. The precision of the drag measurement was less than 2×10^{-4} in this experiment. The force data and physical property of the uniform flow were corrected by the analyzing system of the Digital/Analog-Hybrid Wind Tunnel (DAHWIN)²⁴⁻²⁶ which made it possible to compare the results of CFD and wind tunnel test in real time. The influence of the support and the wing deformation were not eliminated by the corrections.

The model surface has 370 pressure taps: 325 taps on the left and right wings, 12 taps on the fuselage, and 33 taps on horizontal stabilizers. The wing taps are arranged on nine spanwise wing stations ($\eta = 0.131, 0.201, 0.283,$

0.397, 0.502, 0.603, 0.727, 0.846, and .950). The pressure taps are located mainly on the lower surface of the right wing and the upper surface of the left wing. The detailed arrangement of the pressure taps was shown in Ref. 17. To measure the surface pressure, PSI 64-port ESP modules with digital temperature compensation were installed in the model fuselage, and pressure data are acquired by a System 8400.

Oil flow visualization technique was used to investigate the flow pattern on the suction surface of the wing. The oil consisted of silicon oil and fluorescent pigment. Illuminating the ultraviolet light, the photos of the fluorescence from the oil were taken after the test.

II. Results

A. Results of 2D-CRM

1. Lift Coefficient

Hereafter, the physical values of the 2D-CRM experiments, M , C_p , C_L , and AoA , are values after the wind tunnel wall corrections. The uncorrected values are expressed as the setting values.

In the 2D-CRM experiments, lift coefficients were calculated from pressure coefficients C_p in order to evaluate the VGs effect quantitatively. Figure 8 shows the lift coefficient C_L of the 2D-CRM. The vertical and horizontal axes show the C_L and the angle of attack AoA . Closed circle symbols show the C_L of the case without VGs (clean). Other closed and open symbols show the C_L for the cases with VGs of $Hv = 1.2$ mm and 2.4mm, respectively.

In the clean case, the AoA to indicate the maximum C_L was around 3.5 degrees. The C_L of the clean continuously decreased after 3.5 degrees as the AoA increased. When the Dv/Hv was 10 (Red square symbols), the effect of the VGs clearly observed from the C_L curves. The C_L of the $Dv/Hv = 10$ were higher than that of the clean case at the AoA higher than 3.5 degrees. The effect of the VGs decreased as the Dv/Hv increased. The C_L of $Dv/Hv = 20$ (Blue triangle) was smaller than those of $Dv/Hv = 10$. The effect of the VGs had little when the Dv/Hv was 40 (Green diamond).

2. Pressure Coefficient

Figure 9 presents the pressure coefficients C_p in the 2D-CRM experiments. The vertical axis is reversed to show the C_p in the manner that the upper line is the C_p profile on the suction surface. Upper figures show the C_p profiles on the center line. Lower figures show the C_p profile at $x/C = 0.94$ on the suction surface. In Fig. 9, the curves of the C_p at the same setting AoA are shown in the same graph. Because of the correction for the wall interference, the AoA of those cases were a little different from each other.

The characteristics of the C_p profiles on the buffet condition are the decrease of the C_p gradient around the shock wave location and the decrease of the C_p around the trailing edge. Since the instantaneous C_p profiles were averaged in the measurement, the gradient of the C_p around the shock wave location became low when the shock wave oscillated. Because of the flow separation, the C_p around the trailing edge was low on the buffet condition. Those characteristics were confirmed from the comparison between the schlieren movies and the C_p profiles.

At the AoA of 3.36 - 3.45, the shock wave didn't oscillate in all cases. The gradient of the C_p around $x/C = 0.6$ was high and the profile of the C_p at $x/C = 0.94$ was almost flat and high. The difference between the clean and the VGs cases could be observed only in the region around VGs. The C_p of the VGs cases had peak around $x/C = 0.2$ because of the shock wave from the VGs.

At the AoA of 4.30 - 4.57, the C_p of the clean shows the buffet condition. The C_p gradient around $x/C = 0.4$ was low because of the shock wave oscillation. The C_p at $x/C = 0.94$ was not flat. The C_p around $y/b = 0$ decreased because of the flow separation. The VGs suppressed the shock wave oscillation and the flow separation when the Dv/Hv was 10. The C_p profiles of the $Dv/Hv = 10$ were different from that of the clean case. The gradient of C_p was still large around $x/C = 0.5$. The C_p at $x/C = 0.94$ was still almost flat and almost same as that at the AoA of 3.36 - 3.45. In the cases of $Dv/Hv = 20$, the effect of the VGs could be observed from the C_p at $x/C = 0.94$. The profiles of $Dv/Hv = 20$ were higher than that of the clean. The effect of VGs was small when the $Dv/Hv = 40$.

At the AoA of 5.36 - 5.79, the VGs of $Dv/Hv = 10$ and $Hv = 1.2$ mm still suppressed the buffet. The C_p gradient around $x/C = 0.4$ was high. The C_p at $x/C = 0.94$ was still almost flat and almost same as that at the AoA of 3.36 - 3.45 around the center line. The effect of VGs decreased as the Dv/Hv increased. In the case of $Dv/Hv = 20$ and 40, the profiles indicates that the shock wave oscillated on the suction surface.

3. Oil Flow Visualization

The oil flow images on the suction and left side of the airfoil are shown in Fig. 10. In Fig. 10, upper side is upstream and lower side is downstream. Oil flow images were obtained only for the clean case and the VGs case of

$H_v = 1.2$ mm. To show the location of the chord direction, lines and markers were painted on the model at $x/C = 0.3, 0.4, 0.5, 0.6, 0.7, 0.8$, and 0.9 .

In the clean case, an oil line straightly spreads in the spanwise direction around $x/C = 0.5$ at $AoA = 3.37$. From the schlieren images and the pressure data, the straight oil line corresponds to the front of the separation bubble produced by the shock wave. At the $AoA = 4.57$, the straight oil line is still observed. But, the left side of the line is broken. At the $AoA = 5.79$, the straight oil line disappear. So the separation produced by the shock wave was oscillated.

When the D_v/H_v was 10, a characteristic wavy pattern spreads in the spanwise direction around $x/C = 0.5$. The wavy pattern was produced by the interaction between the shock wave and the VGs vortices. From $AoA = 3.45$ to 5.37 , the wavy pattern could be observed. As the D_v/H_v increased, the wavy pattern became unclear. At $AoA = 5.69$, the wavy pattern of $D_v/H_v = 40$ almost disappears.

When the D_v/H_v was 10, the distance between the adjacent vortices was small. Hence the almost region were influenced by the vortices as shown in the wavy pattern of $D_v/H_v = 10$. When the D_v/H_v was 40, the straight lines spread in the spanwise direction between the wavy patterns. Those regions were not affected by the VGs vortices. As shown in Fig. 8, the effect of VGs was large at the $D_v/H_v = 10$ and the effect was little at the $D_v/H_v = 40$. When the VGs vortices do not fill the wing span at the shock wave location, the VGs do not suppress the shock wave oscillation for the 2D-CRM.

4. Schlieren Photographs

Figure 11 shows the schlieren photographs of the clean and the VGs case ($D_v/H_v = 10$ and $H_v = 1.2$ mm). Because of the shock wave oscillation, the shock wave around $x/C = 0.6$ was not observed in the clean case at $AoA = 4.57$ and 5.79 . In the VGs case, the shock wave was clearly observed at $AoA = 4.38$ although the shock wave was a little unclear at $AoA = 5.37$. The VGs suppressed the shock wave oscillation when the D_v/H_v was 10. Although the photos are not shown in Fig. 11, the VGs affected the shock wave oscillation on the schlieren movie even if the D_v/H_v was 40 at $AoA = 4.53$. The shock wave oscillated intermittently in the case.

B. Results of 3D-CRM

1. Aerodynamic Coefficients

Hereafter, the physical values of the 3D-CRM experiments are values after the corrections of the DAHWIN²⁴⁻²⁶. Figure 12 presents lift, drag, and pitching moment coefficients and drag polar of the 3D-CRM. Circle symbols show the case without VGs (Clean). Square, diamond, and triangle symbols show the VGs cases of $D_v/H_v = 20, 40$, and 80 , respectively. The height of the VGs was 0.8 mm in the 3D-CRM experiments. As mentioned above, the ratio of VG's height H_v/δ was 1.5 which was same as that of $H_v = 1.2$ mm in the 2D-CRM experiments.

For all VGs cases, the VGs improved the C_L and the C_m at the high angle of attack. The C_L s of VG cases are higher than that of the clean case. The C_m continuously decreased to about 4.4 degrees. It is important that the VGs for the 3D-CRM maintained their effect from $D_v/H_v = 20$ to 80 . The effect of the VGs on 2D-CRM was little at $D_v/H_v = 40$. So the effect of VGs for the 3D-CRM was much larger than that for the 2D-CRM. The quantitative comparison of the 2D and 3D cases are described in section C.

The C_D increased at low AoA because of the installation drag of the VGs. However, the C_D decreased at high AoA since the separation was suppressed by the VGs. The details of the drag penalty are described in section D.

2. Pressure Coefficient

The pressure coefficient C_p on the wings shows the spatial information of the VGs effect. Figure 13 presents the C_p at $\eta = 0.40, 0.50$, and 0.60 and trailing edge $x/C = 1.0$. At $AoA = 3.0$, the C_p of the clean is a little lower than that of other cases at $x/C = 1.0$ and $\eta = 0.50$. The C_p indicates that the separation started around $\eta = 0.50$ of the trailing edge in the clean case. In the VGs cases, the separation was suppressed at the point.

The effect of VGs are clear at $AoA = 4.0$ and 4.8 . The shock wave position was almost same as that at $AoA = 3.0$ in the VGs cases although the position moved upstream in the clean case. The C_p of the trailing edge decreased from $\eta = -0.73$ to -0.40 in the clean case. The C_p indicates that the separation area around trailing edge increased as the AoA increased in the clean case. In the VGs cases, the C_p was still higher than that in the clean case. The separation was suppressed by the VGs.

3. Oil Flow Visualization

The oil flow images on the suction and right wings are shown in Fig. 14 and Fig. 15. In both figures, upper side is upstream and lower side is downstream. The oil was painted on the wing surface from $x/C = 0.2$ for clean case and $x/C = 0.3$ for VGs cases to avoid the interaction between the oil and the disk roughness and between the oil and the

VGs. Hence, the upper boundary of the oil images is not the line of wing leading edge. White two direction arrows in the images of the clean case show the region where the C_p on the trailing edge decreased from that at the low AoA . So, the arrows roughly show the separation region around the trailing edge. In Fig. 14, the oil flow images of the VGs case of $Dv/Hv = 40$ are shown. Figure 15 shows the oil flow images of the all VGs cases at $AoA = 4.0$.

In Fig. 14, the large separation area appeared in the clean case at $AoA = 4.0$ and 4.8 . The separation area mainly expanded to the outer board from $AoA = 3.0$ to 4.8 . The effect of VGs is clear at these angles. In Fig. 14 and Fig. 15, the large separation area does not appear in the VGs cases. The separation area was segregated by the vortices produced by the VGs.

The trajectory of the vortices can be estimated from lines spreading to the chord direction. As shown in Fig. 15, the interval of the adjacent vortices were large when the $Dv/Hv = 40$ and 80 . In these cases, the VG's vortices did not fill the area of the wing at the shock wave location. In the 2D-CRM experiments, the effect of the VGs was little in such cases. However, the effect of the VGs was clear for the 3D-CRM even if the vortices did not fill the wing.

C. Comparison between 2D- and 3D-CRM

Generally each VG produces installation drag on cruise conditions. Hence small number of VGs and large interval of adjacent VGs are better for the drag penalty. The VGs on the 3D-CRM had a large effect at $Dv/Hv = 80$ although the VGs on the 2D-CRM had little at $Dv/Hv = 40$. The VGs effect on the 3D-CRM is more desirable than that on the 2D-CRM.

In order to quantitatively show the difference between 2D and 3D cases, a rate of increase of the lift coefficient $C_L (= (C_{LVG} - C_{LClean}) / C_{LClean})$ was calculated using the spline interpolation. Figure 16 (a) and (b) show the rate of the C_L increase for the 2D-CRM and the 3D-CRM, respectively. Only the data of $Hv/\delta = 1.5$ are shown for the comparison. The horizontal axis shows the AoA . The values of the low and the high AoA were doubtful because the spline interpolation was used and the number of the points was limited. Hence the low and the high AoA were eliminated from the Fig. 16.

In the 2D-CRM cases, the maximum rate of the C_L increase is over ten percent at $Dv/Hv = 10$. The rate decreased rapidly as the Dv/Hv increased. The rate of $Dv/Hv = 40$ was less than half of the rate of $Dv/Hv = 10$. In the 3D-CRM cases, the rate was about ten percent for all cases. The maximum rate of $Dv/Hv = 40$ was almost same as that of $Dv/Hv = 20$. Although the rate of the $Dv/Hv = 80$ was a little smaller than other cases, the effect of the VGs was clear from Fig. 16 (b).

Figure 17 presents the rate of the C_L increase to the Dv/Hv at the several AoA . The $AoAs$ higher than the buffet conditions were selected in Fig. 17. The lines show exponential approximation curves. As the Dv/Hv increased, the rate rapidly decreased in the 2D cases. However, the rate maintained from the $Dv/Hv = 20$ to 80 in the 3D cases.

Figure 18 shows the enlarged view of the oil flow images of 2D- and 3D-CRM at $Dv/Hv = 40$. The images of 3D-CRM was around $\eta = 0.5$. In the 2D-CRM case, the VG's vortex affected the limited region at the location of the shock wave. Although the oil line curved upstream and downstream on upwash and downwash side of the vortex, the straight oil line spread in the spanwise direction between the vortices. This straight line is similar to the oil line in the clean case and the straight line is the region where the influence of the vortex is little. In the 3D-CRM case, such a straight region could not be observed at the shock wave location. The all region was affected by the vortices and the oil lines mildly curved at the shock wave location. These oil patterns indicate that the influence of the VGs on the 3D-CRM was larger than that on the 2D-CRM.

The effect of the VGs was observed mainly on the mid span of the 3D-CRM. The primal difference between the mid span of the 3D-CRM and the 2D-CRM is sweepback angle. On the swept wings, cross-flow which is perpendicular to the axis of VG vortex appears because of the pressure gradient in the spanwise direction. Hence we considered the difference of the VGs effect between the 2D- and 3D-CRM was mainly caused by the cross-flow.

In the companion paper¹⁰, Ito et al. investigated the influence of the sweepback angle on the VGs effect using CFD. The influence of the sweepback angles was extracted to calculate flow fields on infinite two-dimensional swept wings. The results of the CFD agreed with the experimental results. The toe-out VGs on the swept wings was more effective than the VGs on the unswept wing because the cross-flow around the VG's vortex enhanced the VGs effect. In addition, the surface stream lines of the CFD for unswept and swept wings were similar to the oil flow patterns of 2D- and 3D-CRM experiments shown in Fig. 18. From these results, we concluded that the effect of cross-flow was the main reason of the difference between the 2D- and 3D-CRM. The cross-flow is essentially important for the VGs effect.

D. Penalty of VGs for 3D-CRM

As shown in Fig. 12, the VGs increased the drag coefficient at low AoA . Figure 19 shows the difference between the drag coefficient of the clean and the VGs cases ($C_{DVG} - C_{DClean}$). The horizontal axis shows the lift coefficient C_L . Spline interpolation was used in order to obtain the difference $C_{DVG} - C_{DClean}$.

As shown in Fig. 19, the VGs increased the drag coefficient when the C_L was less than 0.5. The drag increase of $Dv/Hv = 20$ was highest in the three cases. The drag coefficient was decreased by the VGs at the lift coefficient little larger than the design value of 0.5. The VGs suppressed the separation and the effect exceeded the installation drag of the VGs.

The installation drag of VGs ($C_{DVG} - C_{DClean}$) was estimated using the method in Ref. 27. The drag was estimated by the next equations. The several values in these equations can be obtained from the measurement values for the clean case and from the design parameters of VGs.

$$\Delta C_{Dvg} \cong F m_{vg} C_{Dfvg} (S_{vg}/S) \quad (4)$$

$$F = 0.9 \quad (2)$$

$$m_{vg} = 0.60 \left(\frac{U_{vg}}{U_\infty} \right)^{4.2} \left(\frac{U_\infty}{U_{TE}} \right)^{1.0-0.2M_\infty^2} \left(\frac{1+0.2M_\infty^2}{1+0.2M_{TE}^2} \right)^{2.5} \quad (5)$$

$$\frac{U}{U_\infty} = \left\{ 1 - \frac{5}{M_\infty^2} \left[(0.7C_p M_\infty^2 + 1)^{\frac{2}{7}} - 1 \right] \right\}^{\frac{1}{2}} \quad (6)$$

$$M = \left\{ 2.5 \left[\frac{2 + 0.4M_\infty^2}{(0.7C_p M_\infty^2 + 1)^{\frac{2}{7}}} - 2 \right] \right\}^{\frac{1}{2}} \quad (7)$$

$$C_{Dfvg} = C_L \tan \alpha_{vg} \quad (8)$$

$$C_L = (C_L)_{\alpha_{vg}=20} (\alpha_{vg}/20) \quad (9)$$

$$(C_L)_{\alpha_{vg}=20} = 0.3117 + 0.6850AR - 0.2167(AR)^2 \quad (10)$$

$$AR = \frac{2Hv}{Lv} \quad (11)$$

$$S_{vg} = LvHv \quad (12)$$

$$\alpha_{vg} = Av \quad (13)$$

Here, ΔC_{Dvg} is the installation drag of isolated VG. The m_{vg} is a magnification factor for isolated VG on a transonic-transport airplane. C_{Dfvg} is the drag coefficient of isolated VG on a flat plate wing. S_{vg} and S are area of the isolated VG and reference area of the model, respectively. U and M are velocity and Mach number. Subscript TE and vg show the location of trailing edge and vortex generator for those values U and M .

Figure 20 shows the difference between the estimated installation drag $\Delta C_{DEst.}$ and the experimental data $\Delta C_{DExp.}$. The $\Delta C_{DEst.}$ is the total installation drag of VGs. If the estimation is appropriate, the values are close to zero. In Fig. 20, the difference was close to zero when the C_L is larger than 0.35 and lower than 0.50. The estimation method is appropriate for the initial estimation of the installation drag of VGs.

III. Conclusions

Aerodynamic characteristics of two- and three-dimensional NASA common research model (2D-CRM and 3D-CRM) with co-rotating vortex generators (VGs) were investigated for several intervals of adjacent VGs Dv to clarify the influence of the three-dimensionality of the wings on the VGs effect.

In the 2D-CRM experiments, the nominal Mach number of the uniform flow was 0.74 considering the sweepback angle of the 3D-CRM. The nominal Reynolds number was 5×10^6 . The base height of the VGs Hv was 1.5 times of the boundary layer thickness δ at the VGs location. The result of the pressure measurement and the flow

visualization showed the VGs on the 2D-CRM suppressed the buffet and increased the lift when the Dv/Hv was 10. However the VGs had little effect when the Dv/Hv was 40.

In the 3D-CRM experiments, the ratio of Hv/δ was determined as 1.5 in the same way as the 2D-CRM experiment. The direction of the VGs was toe-out which meant the leading edge of the VGs turned to the wing tip. The nominal Mach and Reynolds numbers were 0.85 and 2.27×10^6 , respectively. The VGs on the 3D-CRM increased the lift and suppressed the separation on the wing even if the Dv/Hv was 80.

The comparison between the results of the 2D- and 3D-CRM showed that the effect of the VGs on the 3D-CRM was much larger than that on the 2D-CRM. The rate of the C_L increase to the Dv/Hv rapidly decreased in the 2D-CRM cases as the Dv/Hv increased. However, the rate maintained from the $Dv/Hv = 20$ to 80 in the 3D-CRM cases. From the comparison between the experiments and the CFD results obtained by Ito et al. in the companion paper, we concluded that the difference between 2D- and 3D-CRM was mainly caused by the cross-flow due to the sweepback angles of the 3D-CRM wings. The cross-flow enhances the effect of the co-rotating toe-out VGs on the 3D-CRM wings. The effect of the cross-flow is essentially important for the estimation of the VGs effect.

The penalty of the VGs on the drag coefficient was also investigated in the 3D-CRM experiments. The drag of the 3D-CRM with VGs was higher than that in the clean case when the lift coefficient C_L was less than 0.5. The drag of the 3D-CRM with VGs was lower than that in the clean case when the C_L was higher than 0.5 because the VGs suppressed the separation and the effect exceeded the installation drag of the VGs. The estimation method proposed by Kusunose and Yu was appropriate for the initial estimation of installation drag of VGs.

Acknowledgments

The experiments were conducted in JAXA wind tunnel technology center (WINTeC). The authors would like to thank to the members of WINTeC.

References

- ¹Pearcey, H. H., "Shock-Induced Separation and its Prevention," in Lachmann, G. V. (Ed.), *Boundary Layer and Flow Control, Its Principles and Application*, Vol. 2, Pergamon Press, Oxford, 1961.
- ²Pearcey, H. H. and Holder, D. W., "Examples of the Effects of Shock-Induced Boundary Layer Separation in Transonic Flight," ARC/R&M 3510, 1967.
- ³Engineering Science and Data Unit (ESDU) 93024, "Vortex Generators for Control of Shock-Induced Separation Part1: Introduction and Aerodynamics," 1993.
- ⁴Engineering Science and Data Unit (ESDU) 93025, "Vortex Generators for Control of Shock-Induced Separation Part2: Guide to Use of Vane Vortex Generators," 1994.
- ⁵Engineering Science and Data Unit (ESDU) 93026, "Vortex Generators for Control of Shock-Induced Separation Part3: Example of Applications of Vortex Generators to Aircraft," 1995.
- ⁶Koike, S., Sato, M., Kanda, H., Nakajima, T., Nakakita, K., Kusunose, K., Murayama, M., Ito, Y., and Yamamoto, K., "Experiment of Vortex Generators on NASA SC(2)-0518 Two Dimensional Wing for Buffet Reduction," Proceedings of the 2013 Asia-Pacific International Symposium on Aerospace Technology, Takamatsu, Japan, Nov.20-22, 2013.
- ⁷Koike, S., Sato, M., Kanda, H., Nakajima, T., Nakakita, K., Kusunose, K., Murayama, M., Ito, Y., and Yamamoto, K., "Effect of Vortex Generators on Two-Dimensional Wings in Transonic Flows," JAXA Research and Development Report, JAXA-RR-14-002, 2014 (in Japanese).
- ⁸Ito, Y., Murayama, M. and Yamamoto, K., "High-Quality Unstructured Hybrid Mesh Generation for Capturing Effects of Vortex Generators," AIAA Paper 2013-0554, 51st AIAA Aerospace Sciences Meeting Including the New Horizons Forum and Aerospace Exposition, Grapevine, TX, January 2013, DOI: 10.2514/6.2013-554.
- ⁹Ito, Y., Murayama, M. and Yamamoto, K., "Efficient and Accurate Evaluation of Aircraft in Different Configurations with Automatic Local Remeshing," AIAA Paper 2013-2711, 21st AIAA Computational Fluid Dynamics Conference, San Diego, CA, June 2013, DOI: 10.2514/6.2013-2711.
- ¹⁰Ito, Y., Yamamoto, K., Kusunose, K., Koike, S., Nakakita, K., Murayama, M., and Tanaka, K., "Effect of Vortex Generators on Transonic Swept Wings," 53rd AIAA Aerospace Sciences Meeting, Kissimmee, FL, January 2015, to be presented.
- ¹¹CRM.65.airfoil sections, <http://commonresearchmodel.larc.nasa.gov/crm-65-airfoil-sections/> [cited 24 June 2014].
- ¹²Vassberg, J., Dehaan, M., Rivers, M. and Wahls, R., "Development of a Common Research Model for Applied CFD Validation Studies," AIAA Paper 2008-6919, 26th AIAA Applied Aerodynamics Conference, Honolulu, HI, 2008, DOI: 10.2514/6.2008-6919.
- ¹³NASA Common Research Model, <http://commonresearchmodel.larc.nasa.gov/> [cited 24 June 2014].
- ¹⁴Ueno, M., Kohzai, M., Koga, S., Kato, H., Nakakita, K. and Sudani, N., "80% Scaled NASA Common Research Model Wind Tunnel Test of JAXA at Relatively Low Reynolds Number," AIAA Paper 2013-0493, 51st AIAA Aerospace Sciences Meeting Including the New Horizons Forum and Aerospace Exposition, Grapevine, TX, 2013, DOI: 10.2514/6.2013-493.

- ¹⁵Koga, S., Kohzai, M., Ueno, M., Nakakita, K. and Sudani, N., "Analysis of NASA Common Research Model Dynamic Data in JAXA Wind Tunnel Tests," AIAA Paper 2013-0495, 51st AIAA Aerospace Sciences Meeting Including the New Horizons Forum and Aerospace Exposition, Grapevine, TX, 2013, DOI: 10.2514/6.2013-495.
- ¹⁶Kohzai, M., Ueno, M., Koga, S. and Sudani, N., "Wall and Support Interference Corrections of NASA Common Research Model Wind Tunnel Tests in JAXA," AIAA Paper 2013-0963, 51st AIAA Aerospace Sciences Meeting Including the New Horizons Forum and Aerospace Exposition, Grapevine, TX, 2013, DOI: 10.2514/6.2013-963.
- ¹⁷Ueno, M., Kohzai, T., and Koga, S., "Transonic Wind Tunnel Test of the NASA CRM (Volum1)," JAXA Research and Development Memorandum, JAXA-RM-13-017E, 2014.
- ¹⁸Harris, C. D., "NASA Supercritical Airfoils—a Matrix of Family-Related Airfoils," NASA Technical Paper 2969, 1990.
- ¹⁹Braslow, A. L., and Knox, E. C., "Simplified Method for Determination of Critical Height of Distributed Roughness Particles for Boundary-Layer Transition at Mach Numbers from 0 to 5," NACA-TN-4363, 1958.
- ²⁰Second Aerodynamics Division Staff "Construction and Performance of NAL Two-Dimensional Transonic Wind Tunnel," National Aerospace Lab., Rept. TR-647T, 1982 (in Japanese).
- ²¹Two-Dimensional Transonic Wind Tunnel Staff "Revitalization of NAL Two-Dimensional Transonic Wind Tunnel," National Aerospace Lab., Rept. TM-744, 1999 (in Japanese).
- ²²Sawada, H., "A General Correction Method of the Interference in 2-Dimensional Wind Tunnels with Ventilated Walls," *Transactions of the Japan Society for Aeronautical and Space Sciences*, Vol. 21, No.52, 1978, pp. 57-68.
- ²³Sawada, H., Sakakibara, S., Sato, M., and Kanda, H., "Wall Interference Estimation of the NAL's Two-Dimensional Wind Tunnel," National Aerospace Lab., Rept. TR-829, 1984 (in Japanese).
- ²⁴Kawamoto, I., Oguni, Y., Nakamura, S., and Hosoe, N., "Corrections to the Experimental Data of the NAL-TWT –Mach Number and Buoyancy Corrections," Proceedings of 30th fluid dynamics conference, 1998, pp. 365-368 (in Japanese).
- ²⁵Kohzai, M., Ueno, M., Shiohara, T., Komatsu, Y., Karasawa, T., Koike, A., Sudani, N., Ganaha, Y., Kon, N., Haraguchi, T., and Nakamura, A., "Calibration of the test section Mach number in the JAXA 2m x 2m Transonic Wind Tunnel," Proceedings of the Wind Tunnel Technology Association 77th meeting, JAXA Special Publication, JAXA-SP-06-026, 2007, pp. 6-14 (in Japanese).
- ²⁶Hidaka, A., Kuchiishi, S., Koike, A., Kohzai, M., and Morita, Y., "Wall Interference Correction by the Panel Method for the JAXA 2m x 2m Transonic Wind Tunnel," JAXA Research and Development Report, JAXA-RR-07-033, 2007 (in Japanese).
- ²⁷Kusunose, K. and Yu, N. J., "Vortex Generator Installation Drag on an Airplane near Its Cruise Condition," *Journal of Aircraft*, Vol. 40, No. 6, 2003, pp. 1145-1151, DOI: 10.2514/2.7203.

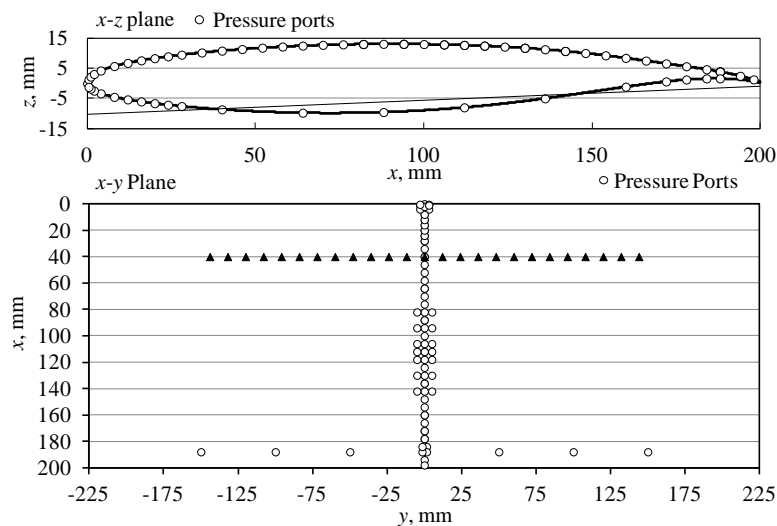


Figure 1. Schematic of 2D-CRM. Circle symbols show the pressure taps. Triangle symbols show the vortex generators of $Dv/Hv = 10$.

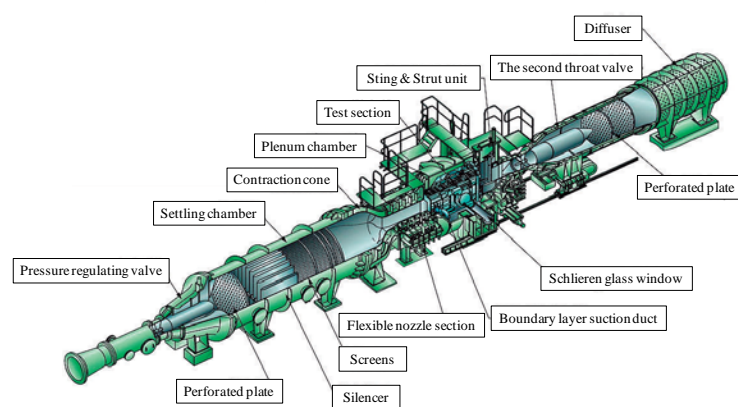


Figure 2. Bird eye view of JAXA 0.8m x 0.45m high Reynolds number transonic wind tunnel (JTWT2).

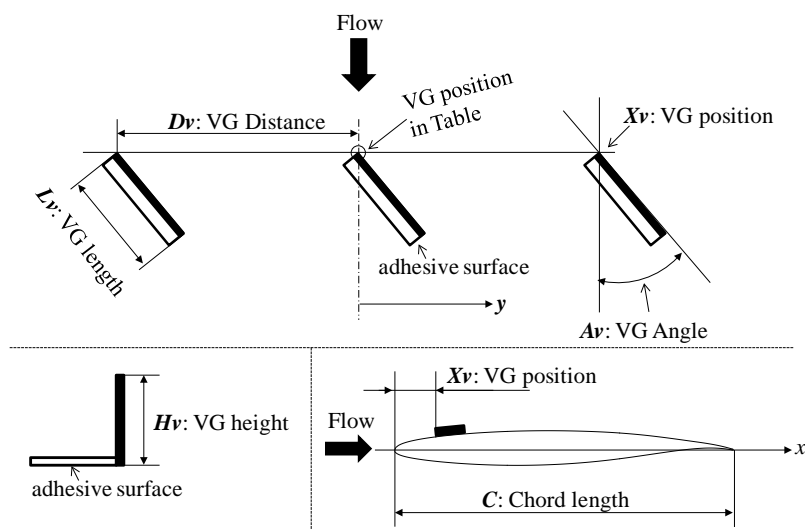


Figure 3. Parameters of vortex generators.

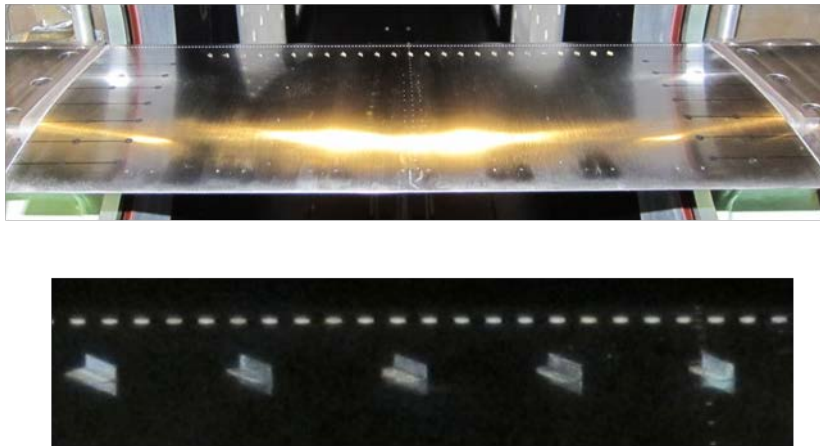


Figure 4. Photos of 2D-CRM with vortex generators.

Table 1. Parameters of 2D-CRM experiments.

Experimental conditions	H_v , mm	H_v/δ^{*1}	D_v , mm	D_v/H_v	A_v , deg	X_v/C	L_v/H_v (AR)
VG1.2mm12mm20deg20% AR4	1.2	1.5	12	10	20	0.2	4
VG1.2mm24mm20deg20% AR4	1.2	1.5	24	20	20	0.2	4
VG1.2mm48mm20deg20% AR4	1.2	1.5	48	40	20	0.2	4
VG2.4mm24mm20deg20% AR4	2.4	3.0	24	10	20	0.2	4
VG2.4mm48mm20deg20% AR4	2.4	3.0	48	20	20	0.2	4
VG2.4mm96mm20deg20% AR4	2.4	3.0	96	40	20	0.2	4

^{*1} δ is boundary layer thickness estimated from CFD results.

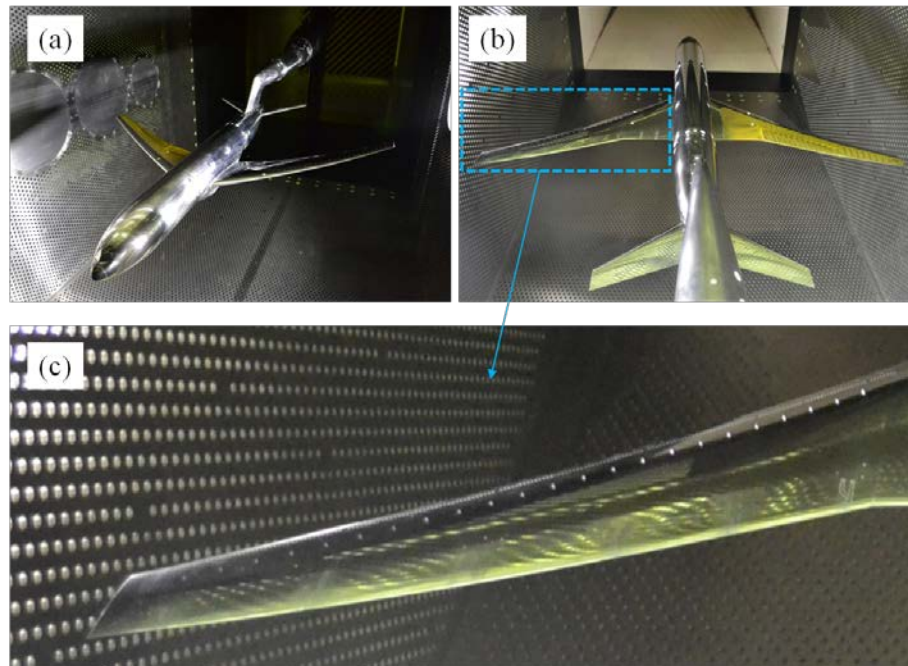


Figure 5. Photos of JAXA's 80% scale NASA CRM (3D-CRM) with vortex generators.

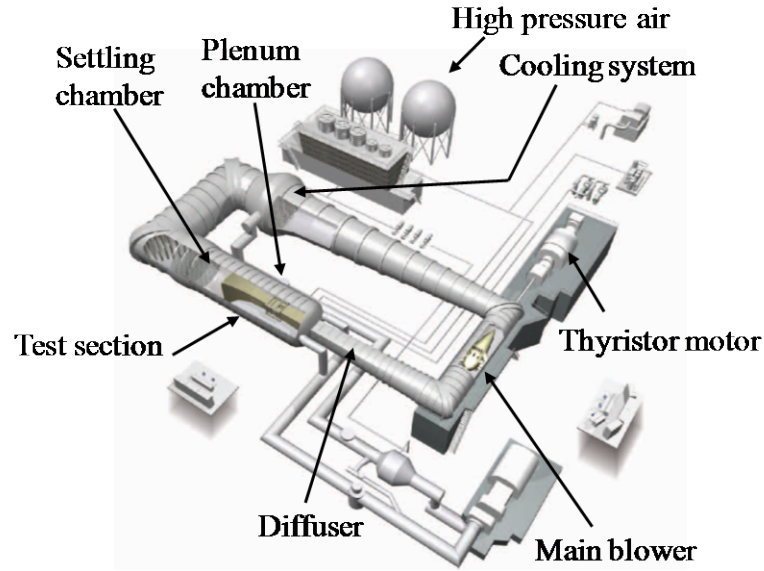


Figure 6. Bird eye view of JAXA 2m x 2m transonic wind tunnel (JTWT).

Table 2. Parameters of 3D-CRM experiments.

Experimental conditions	H_v , mm	H_v/δ	D_v , mm	D_v/H_v	A_v , deg ^{*2}	VG direction	X_v/C ^{*3}	L_v/H_v (AR)	η	N_{VG} ^{*4}
VG0.8mm16mm20deg20% AR4	0.8	1.5	16	20	20	Toe-out	about 0.2	4	0.4 - wing tip	23
VG0.8mm32mm20deg20% AR4	0.8	1.5	32	40	20	Toe-out	about 0.2	4	0.4 - wing tip	12
VG0.8mm64mm20deg20% AR4	0.8	1.5	64	80	20	Toe-out	about 0.2	4	0.4 - wing tip	6

^{*1} δ is boundary layer thickness estimated from CFD results.

^{*2} A_v shows VGs angle to the flow direction on a main wing. Angle to the body axis is 32.6 degrees.

^{*3} X_v/C is depend on the η . X_v/C in the table shows the location on the outboard.

^{*4} N_{VG} is the number of VGs on a half wing.

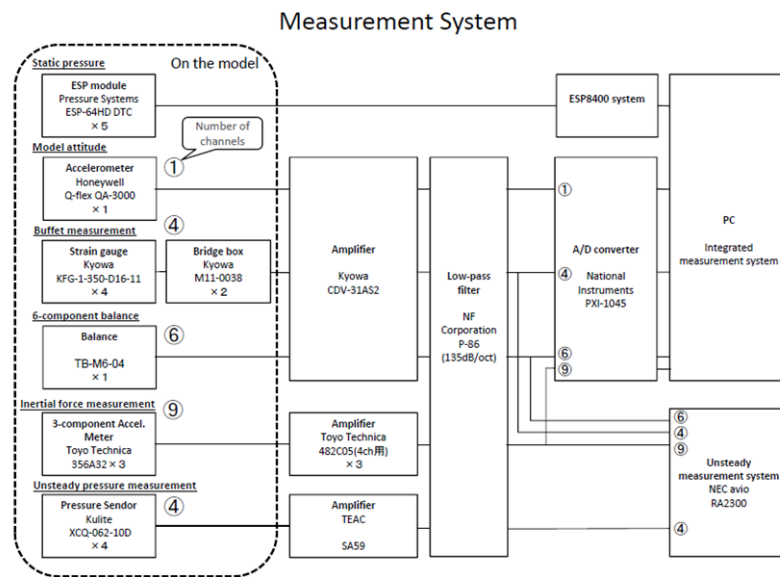


Figure 7. Measurement system of JAXA's 80% scale NASA CRM (3D-CRM).

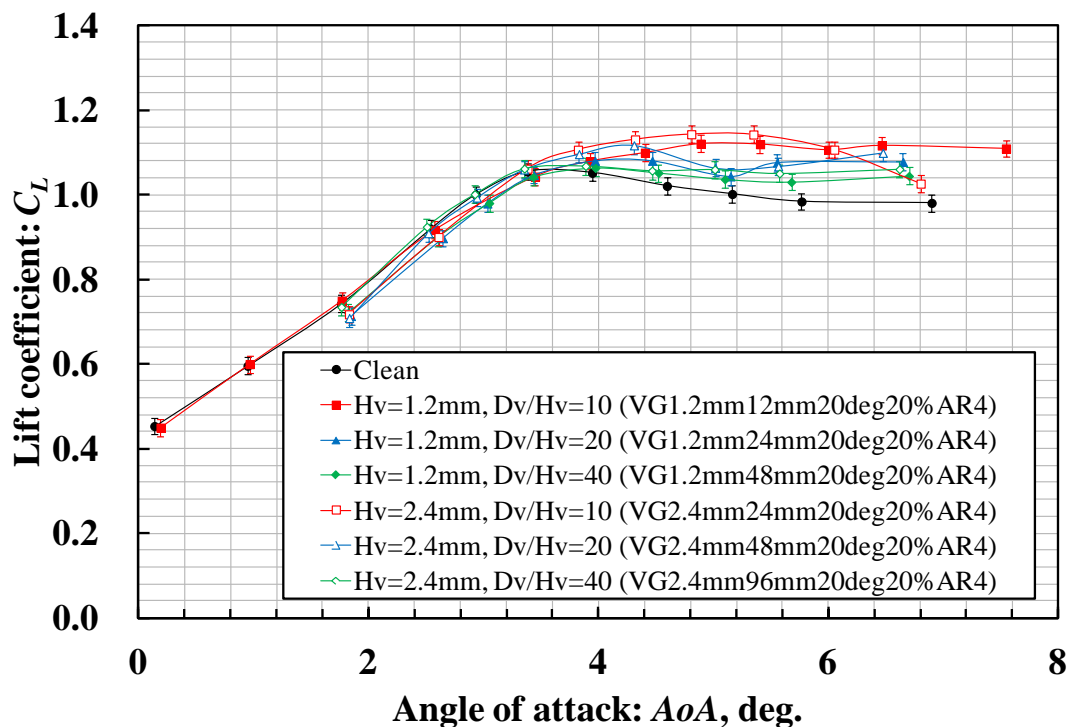


Figure 8. Lift coefficient of 2D-CRM experiment.

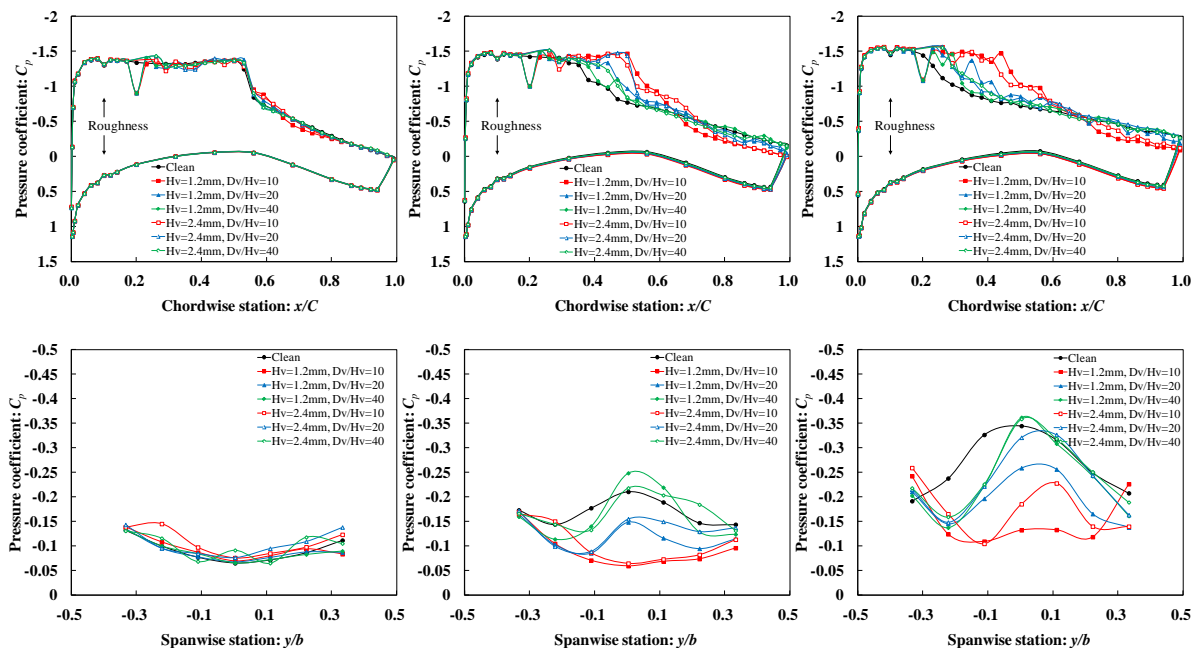


Figure 9. Lift coefficient of 2D-CRM experiment.

Left: $AoA = 3.36 - 3.45$, Middle: $AoA = 4.30 - 4.57$, Right: $5.36 - 5.79$. (Setting $AoA = 5, 6, 7$)
Upper: $y = 0$ mm, Lower: $x/C = 0.94$.

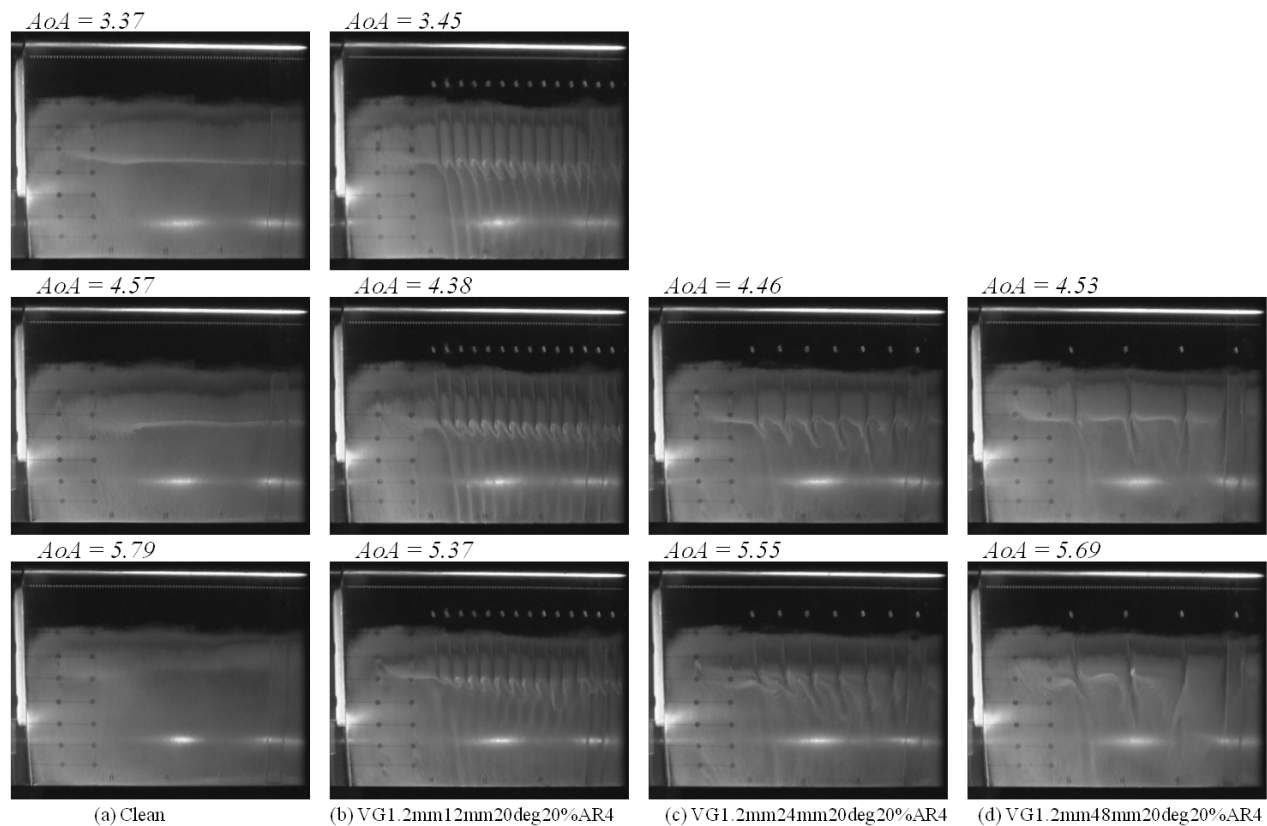


Figure 10. Oil flow images of 2D-CRM experiment.

(a) Clean, (b) $Hv=1.2mm$, $Dv/Hv=10$, (c) $Hv=1.2mm$, $Dv/Hv=20$, (d) $Hv=1.2mm$, $Dv/Hv=40$.

Setting $AoA = 5, 6, 7$. Caption show the corrected AoA .

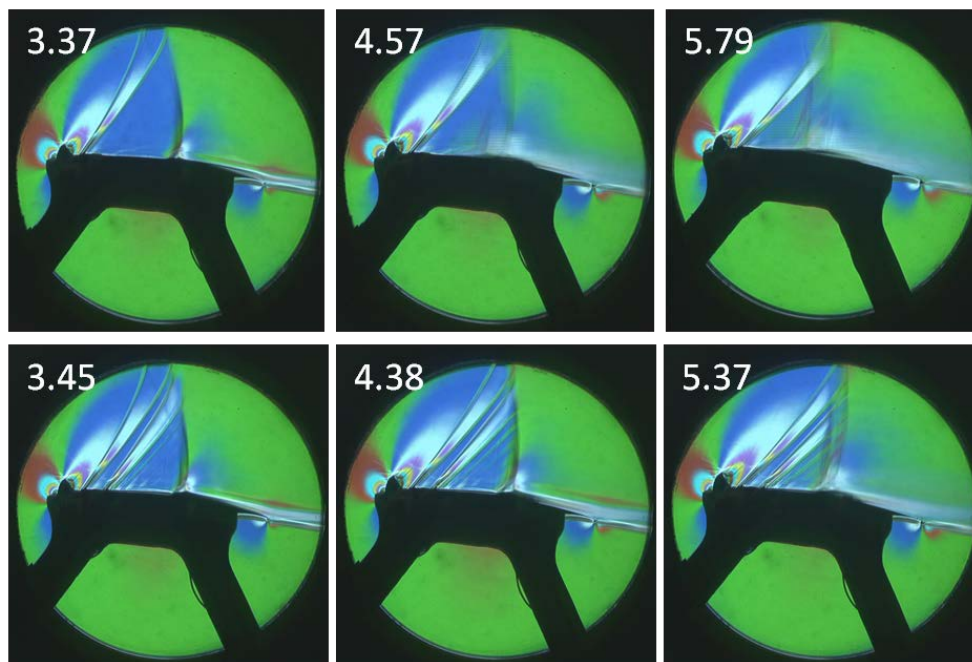


Figure 11. Schlieren photographs of 2D-CRM.

Upper: Clean, Lower: $Hv = 1.2mm$, $Dv/Hv = 10$, Setting $AoA = 5, 6, 7$. Captions show the corrected AoA .

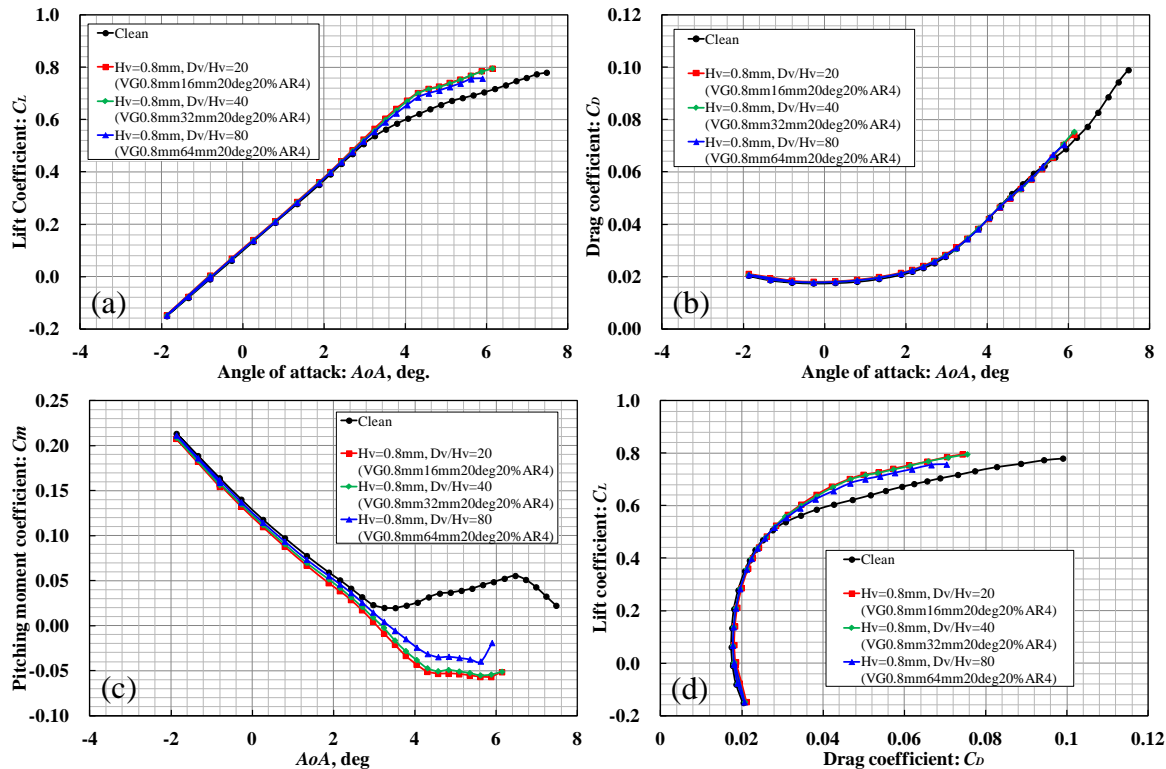


Figure 12. Aerodynamic coefficients of 3D-CRM with and without VGs.
 (a) Lift coefficient, (b) drag coefficient, (c) Pitching moment coefficient, (d) drag polar.
 Black: Clean, Red: Dv/Hv=20, Green: Dv/Hv=40, Blue: Dv/Hv=80.

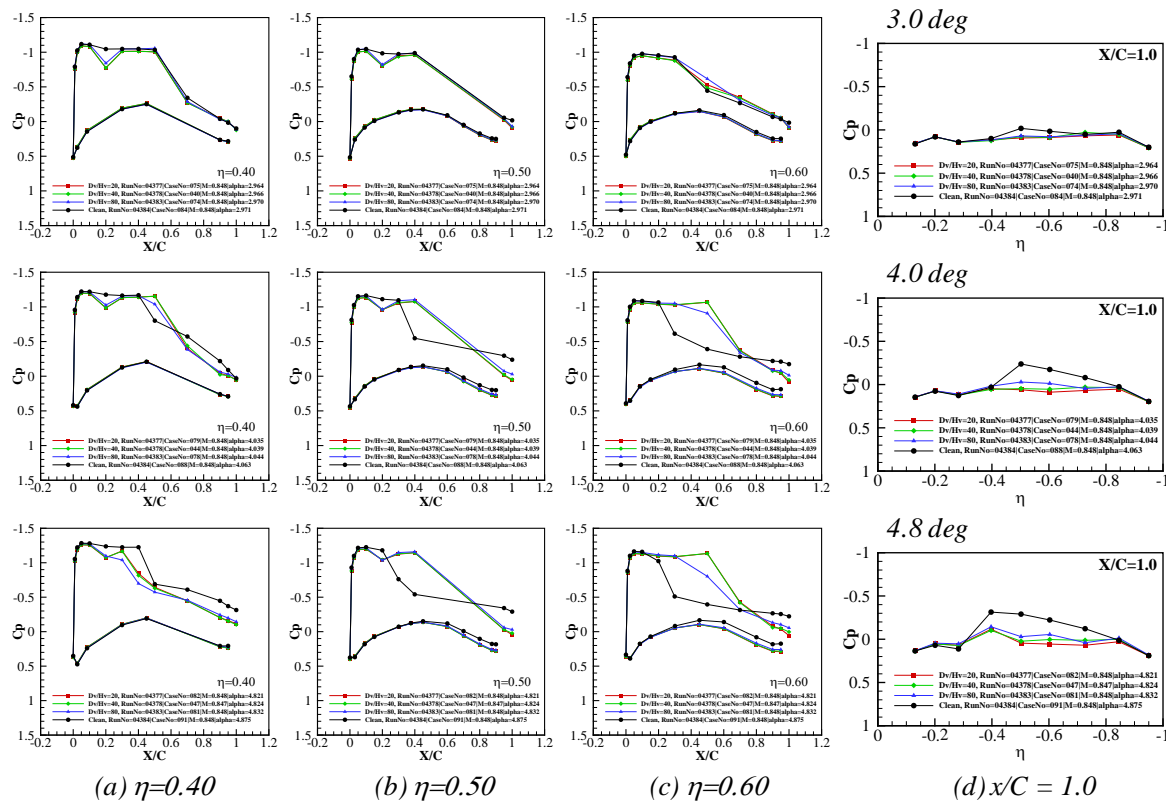


Figure 13. Pressure coefficient of 3D-CRM. $\eta = 0.40, 0.50$, and 0.60 . $x/C = 1.0$ (trailing edge).

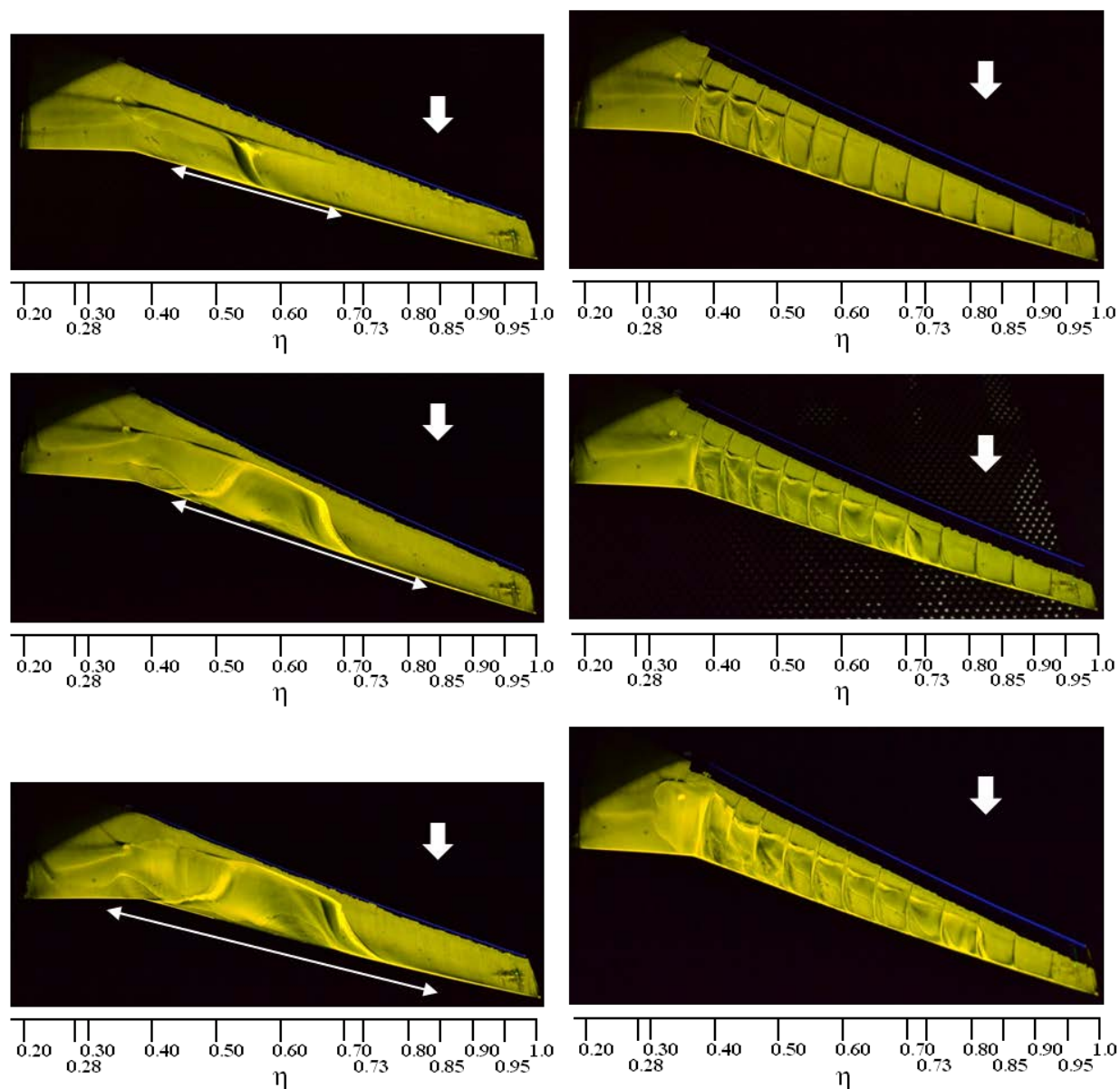


Figure 14. Oil flow images of 3D-CRM.
Upper: AoA = 3.0, Middle: AoA = 4.0, Lower: AoA = 4.8
Left: Clean, Right: Dv/Hv=40

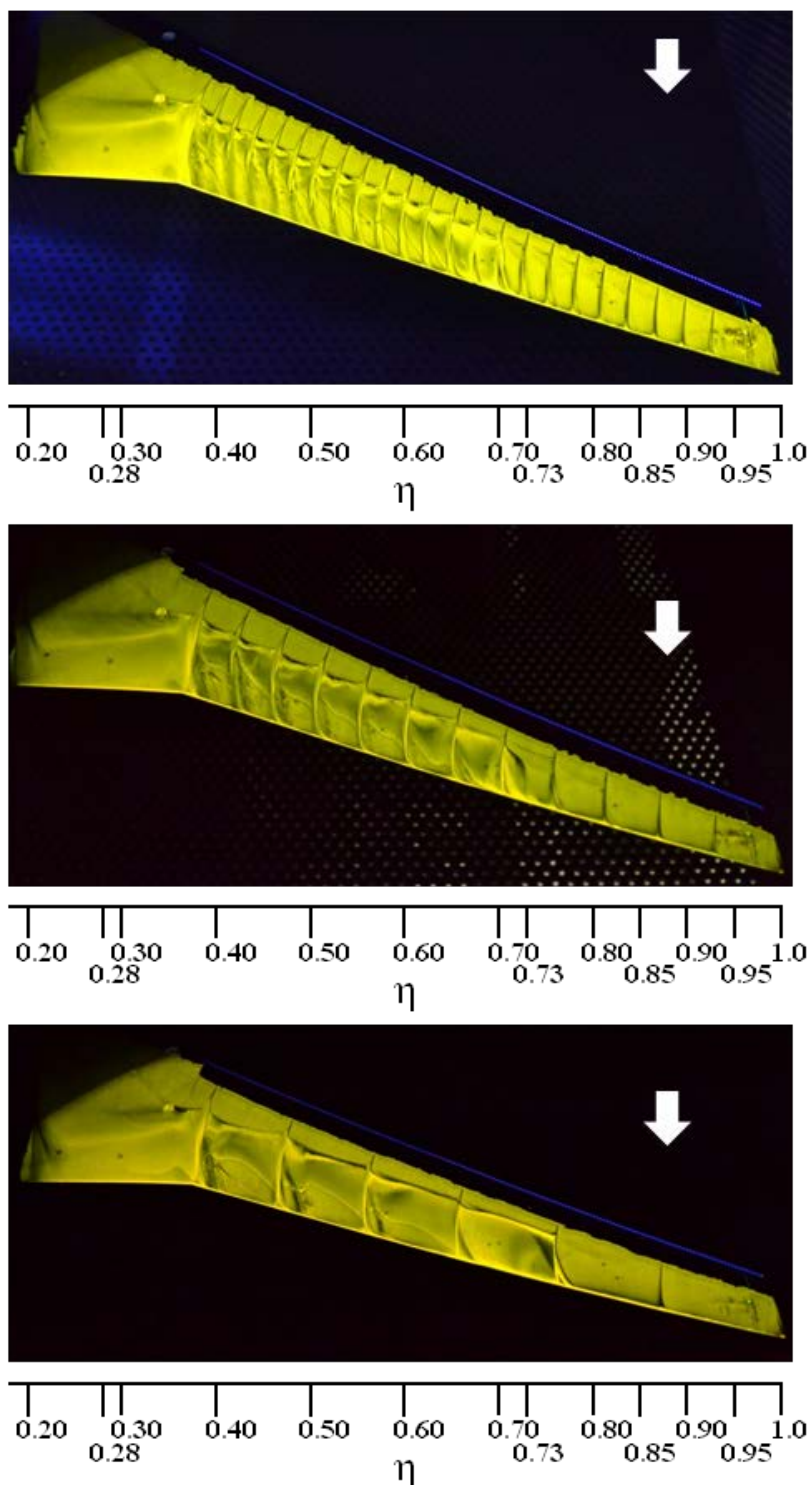
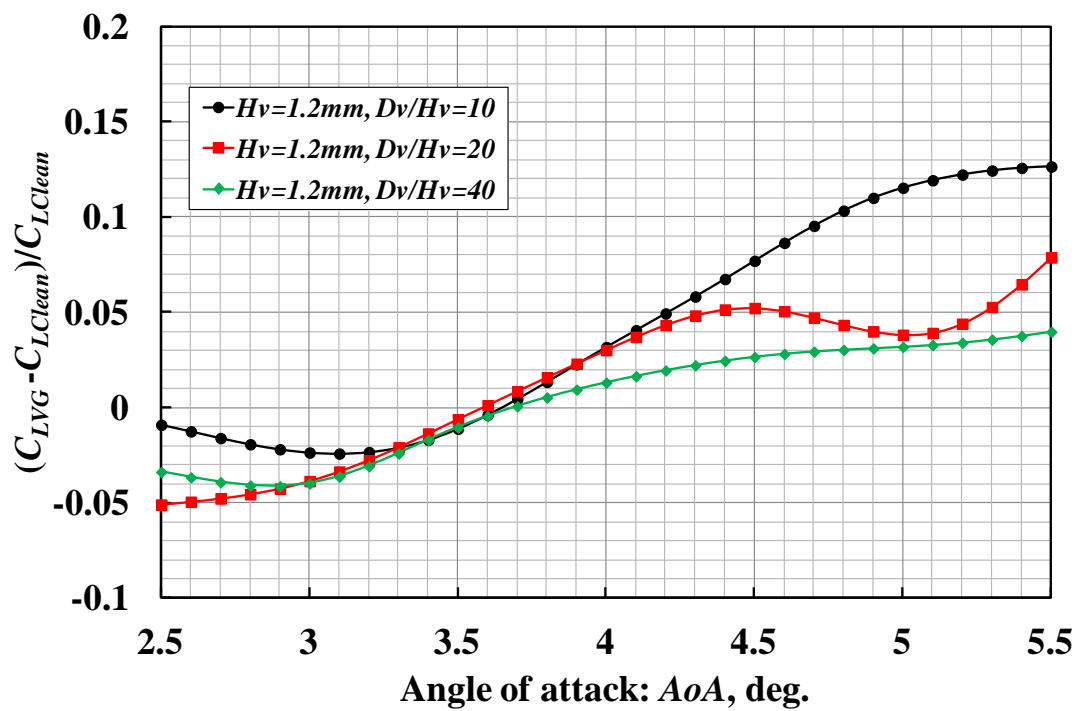
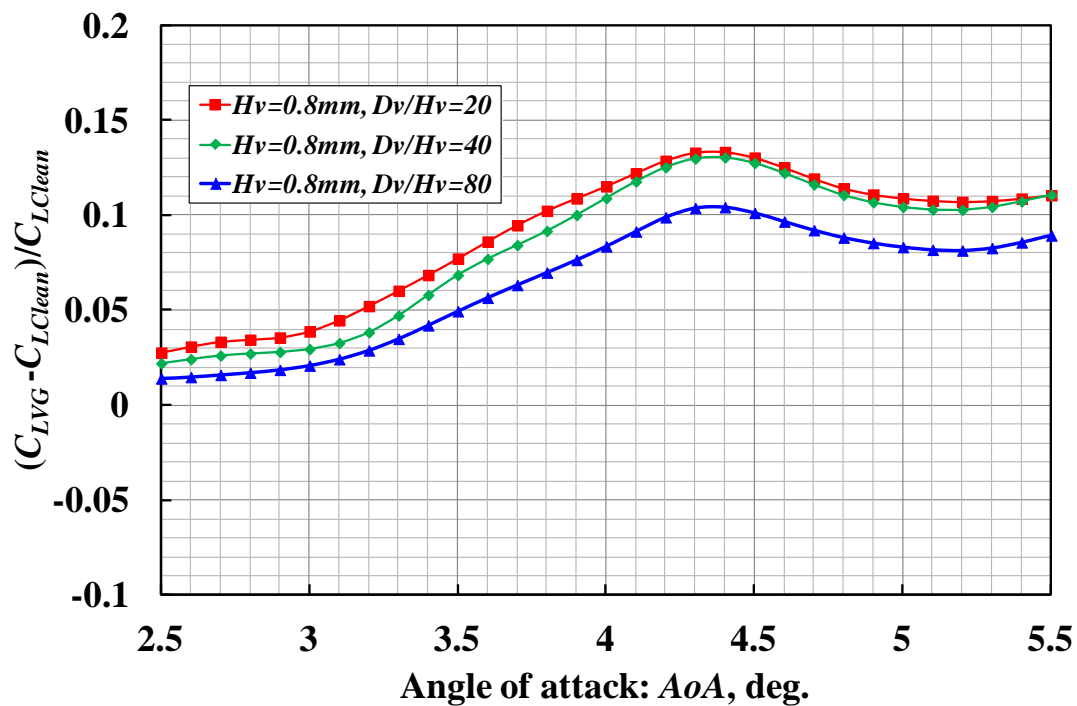


Figure 15. Oil flow images of 3D-CRM with VGs.
Upper: $Dv/Hv = 20$, Middle: $Dv/Hv = 40$, Lower: $Dv/Hv = 80$, $AoA = 4.0$



(a) 2D-CRM



(b) 3D-CRM

Figure 16. Rate of increase of lift coefficient to AoA.
 Black: $D_v/H_v = 10$, Red: $D_v/H_v = 20$, Green $D_v/H_v = 40$, Blue: $D_v/H_v = 80$.

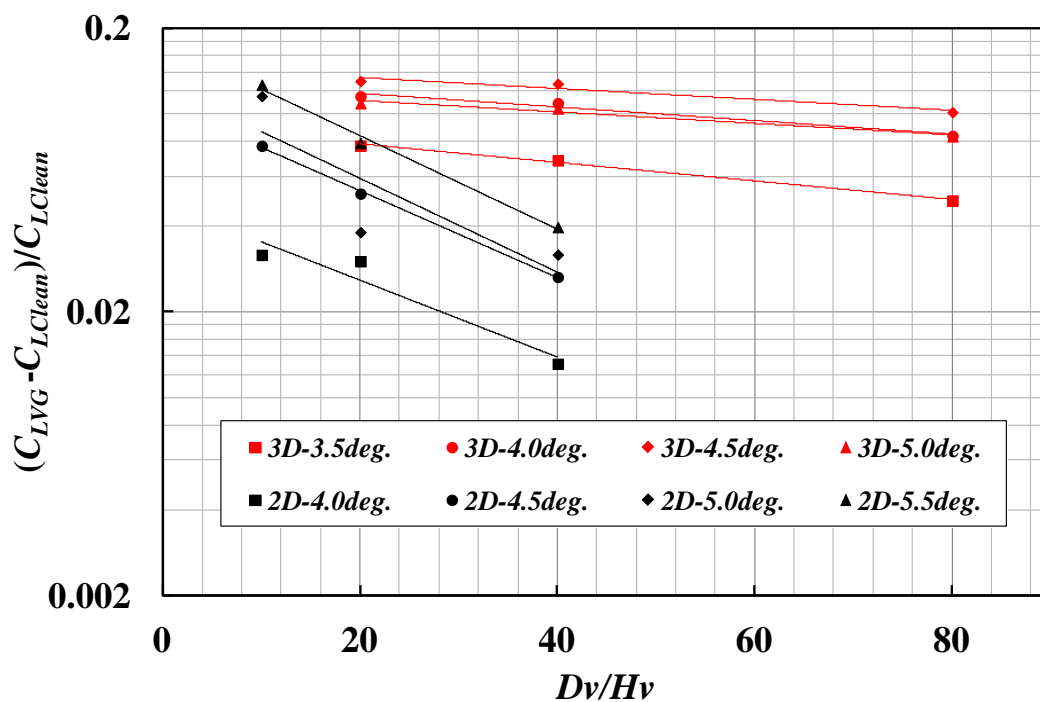


Figure 17. Rate of increase of lift coefficient to Dv/Hv .
Black: 2D-CRM, Red: 3D-CRM

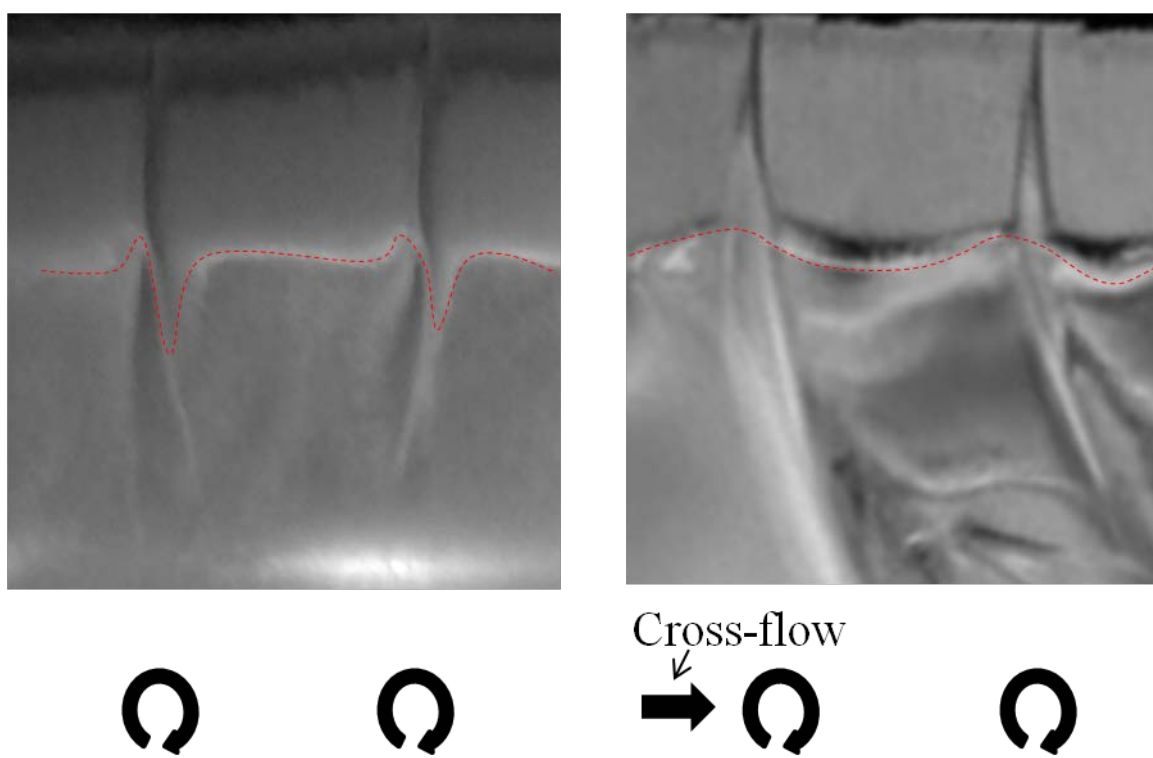


Figure 18. Enlarged view of oil flow images around shock wave.
Left: 2D-CRM ($AoA = 4.4$), Right: 3D-CRM around $\eta = 0.5$ ($AoA = 4.0$).
Red broken lines show oil pattern produced by separation at the location of the shock wave.
Lower figures show the direction of VGs vortices from the view point of downstream.

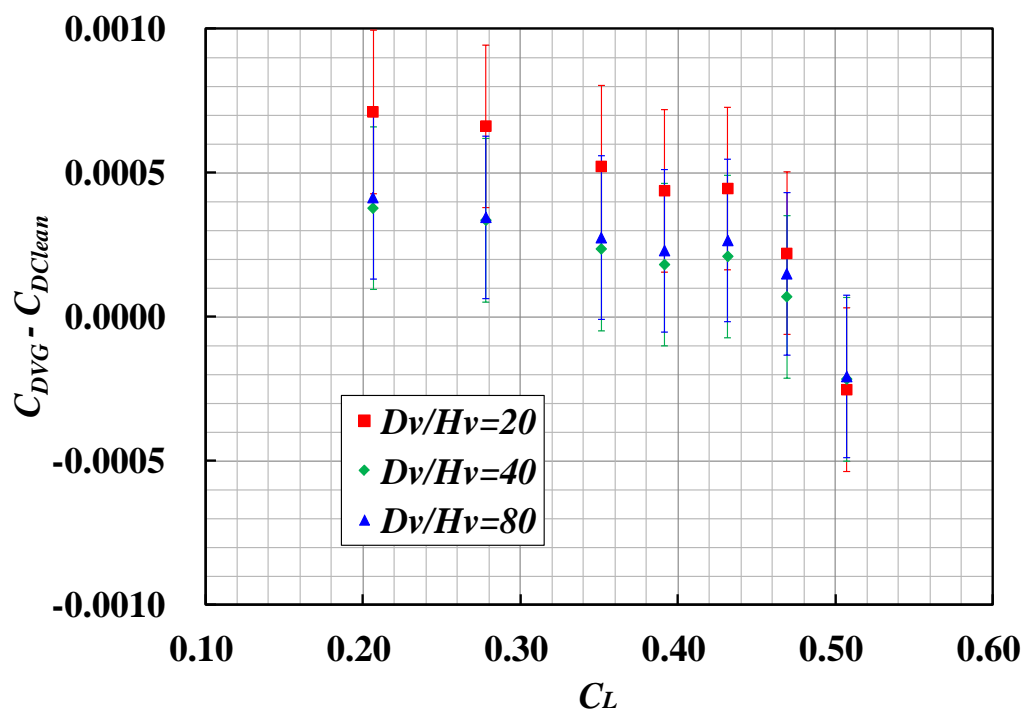


Figure 19. Difference of drag coefficient with and without VGs.
Bands show the uncertainty from the measurement error of drag coefficient.

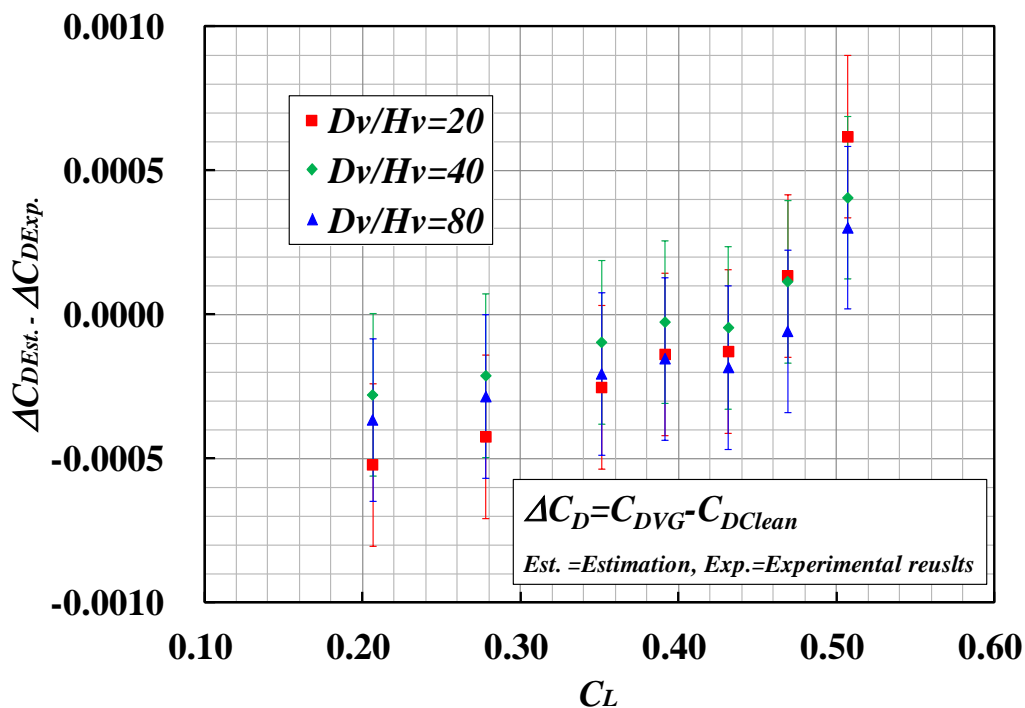


Figure 20. Difference of experimental and estimated drag coefficient.
Bands show the uncertainty from the measurement error of drag coefficient.